[2]Bloor, S., "The Transition to Turbulence in the Wake of a Circular Cylinder," *Journal of Fluid Mechanics*, Vol. 19, 1963, pp. 290–303.

[3]Koutra, A., Boisson, H. C., Chassaing, P., and Ha Minh, H., "Non Linear Interaction and the Transition to Turbulence in the Wake of a Circular Cylinder," *Journal of Fluid Mechanics*, Vol. 181, 1987, pp. 141–161.

[4]Wei, T., and Smith, C. R., "Secondary Vortices in the Wake of Circular Cylinders," *Journal of Fluid Mechanics*, Vol. 169, 1986, pp. 513–533.

[5]Prasad, A., and Williamson, C. H. K., "The Instability of the Shear Layer Separating from a Bluff Body," *Journal of Fluid Mechanics*, Vol. 333, 1997, pp. 375–402.

[6]Ahmed, N. A., and Archer, R. D., "Post-Stall Behavior of a Wing Under Externally Imposed Sound," *Journal of Aircraft*, Vol. 38, No. 5, 2001, pp. 961–963.

[7]Gatto, A., Ahmed, N. A., and Archer, R. D., "Investigation of the Upstream End Effect of the Flow Characteristics of a Yawed Circular Cylinder," *Aeronautical Journal of the Royal Aeronautical Society*, Vol. 104, No. 1033, 2000, pp. 125–128.

[8]West, G. S., and Apelt, C. J., "The Effects of Tunnel Blockage and Aspect Ratio on the Mean Flow past a Circular Cylinder with Reynolds Number Between 10^4 and 10^5," *Journal of Fluid Mechanics*, Vol. 114, 1982, pp. 361–377.

[9]Kovasznay, L. S. G., "Hot Wire Investigation of the Wake Behind Cylinders at Low Reynolds Numbers," *Proceedings of the Royal Society of London, Series A*, Vol. 198, July–Sept. 1949, pp. 174–190.

[10]Szepessey, S., and Bearman, P. W., "Aspect Ratio and End Plate Effects on Vortex Shedding from a Circular Cylinder," *Journal of Fluid Mechanics*, Vol. 234, 1992, pp. 191–217.

[11]Ho, C. H., and Huerre, P., "Perturbed Free Shear Layers," *Annual Review of Fluid Mechanics*, Vol. 16, 1984, pp. 365–424.

[12]Roshko, A., "Structure of Turbulent Shear Flows: A New Look," *AIAA Journal*, Vol. 14, No. 10, 1976, pp. 1349–1357.

[13]Unal, M. F., and Rockwell, D., "On Vortex Formation from a Cylinder. Part 2: The Initial Instability," *Journal of Fluid Mechanics*, Vol. 190, 1988, pp. 513–528.

W. J. Devenport
Associate Editor

Vortex Breakdown–Tail Interaction

Y. Kim,* M. Ozgoren,† and D. Rockwell‡
Lehigh University, Bethlehem, Pennsylvania 18015

Introduction

THE impingement of a broken-down vortex on a tail is part of a larger framework of vortex-body interactions, as reviewed by Rockwell.[1] The buffeting of the tail of an F-series aircraft is well known and has been investigated from a variety of perspectives in recent years. This interaction may be associated with several forms of unsteadiness: nonperiodic displacements of the entire vortex core,[2] a helical-mode instability of the broken-down vortex,[3,4] and streamwise fluctuations of the region of vortex breakdown.[5] A variety of qualitative flow visualizations, usually in conjunction with unsteady loading characteristics of the tail, have been pursued in recent years. Fewer studies, however, have quantitatively addressed the major features of the flow. Beutner et al.[6] determined the rms variations of fluctuating quantities of the flowfield, and Canbazoglu et al.[7,8] provide instantaneous and averaged representations of the flow structure. Related numerical investigations include the works of Rizk and Gee,[9] Gee et al.,[10] Kandil et al.,[11] and Rizzetta.[12] Certain features of the vortex breakdown–tail interaction can be simulated experimentally by vortex encounter with a flat plate having a zero sweep angle, as shown by Wolfe et al.[13] and Mayori and Rockwell.[14] The corresponding computations by Gordnier and Visbal[15] fully accounted for the instantaneous and time-averaged flow structure, in three-dimensional form.

Particularly relevant to the present investigation are the works of Washburn et al.[16] and Canbazoglu et al.[8] Both of these investigations detected not only a primary (incident) vortex along the tail, but also a secondary (counter) vortex that was generally attributable to some type of vortex generation in the leading region of the tail; the physics of the onset of the secondary vortex, however, were not addressed. Although certain aspects of the fluctuating vorticity field were preliminarily characterized by Canbazoglu et al.,[8] the fluctuating velocity fields, which are essential for characterizing the origin of buffet loading of the tail, have not been addressed. Furthermore, the physical origin of these velocity fluctuations is intimately related to the Reynolds stress, which also has not been provided.

The aim of this investigation is to address these unclarified issues and to interpret them physically using a technique of high-image-density particle image velocimetry.

Experimental System and Techniques

Experiments were performed in a large-scale water channel to allow effective imaging of the flow structure. The water channel had a test section that was 5000 mm long, 927 mm wide, and 610 mm deep. The water level was maintained at an elevation of 559 mm. The delta wing–tail system was mounted upside down within a false wall unit to optimize the imaging of the flow structure. The spanwise width between false walls was 510 mm, and the length of these walls was 590 mm.

The dimensions of the delta wing and tail are illustrated in Fig. 1. The wing had a chord C of 342 mm and a thickness-to-chord ratio $t_w/C = 0.028$. The sweep angle of the wing was $\Lambda = 75$ deg. The effective sweep angle of the center of the leading-edge vortex was $\lambda_L = 79$ deg. For all experiments, the angle of attack of the wing was maintained at $\alpha = 21$ deg. The freestream velocity was $U = 152$ mm/s. The Reynolds number based on C was $Re = 5.2 \times 10^4$.

The root chord of the tail was $C_T = 105$ mm; its thickness-to-chord ratio was $t_T/C_T = 0.12$. Both the leading and tip edges of the tail were beveled at an angle of 30 deg. The span of the swept leading edge of the tail was $S_T = 136$ mm, and the angles of inclination

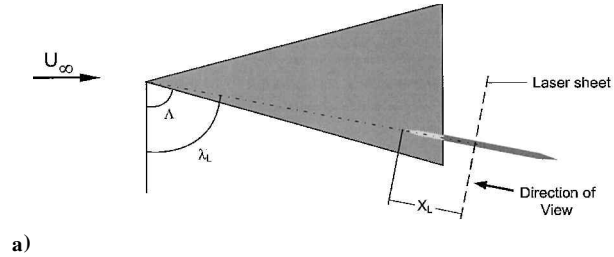

a)

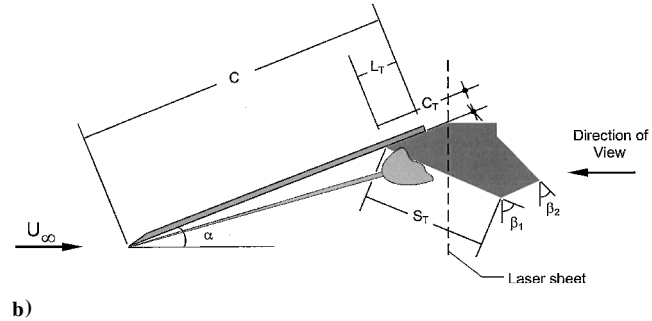

b)

Fig. 1 Schematic of a) plan and b) side views of delta wing–tail arrangement.

Received 19 June 2002; revision received 11 October 2002; accepted for publication 24 October 2002.

*Research Associate, Department of Mechanical Engineering and Mechanics, 354 Packard Laboratory, 19 Memorial Drive West.

†Visiting Scholar, Department of Mechanical Engineering and Mechanics, 354 Packard Laboratory, 19 Memorial Drive West.

‡Paul B. Reinhold Professor, Department of Mechanical Engineering and Mechanics, 354 Packard Laboratory, 19 Memorial Drive West. Member AIAA.

of the leading and trailing edges of the tail were $\beta_1 = 70$ deg and $\beta_2 = 45$ deg. Further details of the tail geometry are provided by Canbazoglu et al.[7] The leading edge of the tail was located at a distance $L_T/C_T = 0.047$ upstream of the trailing edge of the delta wing. The tail was mounted on the delta wing such that its plane was coincident with the centerline of the incident, broken-down vortex. Both the delta wing and the tail were held in position using thin struts extending vertically through the free surface of the water channel.

A technique of high-image-density particle image velocimetry was used to determine the instantaneous velocity field at an effective frame rate of 15 frames per second. These velocity fields were determined over four, sequential crossflow planes, designated in Fig. 2 as planes *A*, *B*, *C*, and *D*. These planes were located at streamwise distances $X_L = 0.108, 0.612, 0.965$, and $1.25\,C_T$, according to the definitions of Fig. 1. Laser illumination was provided by a dual pulsed Yag system that yielded 90 mJ per pulse. The pulses had time delay of $\Delta t = 67$ ms. The flow was seeded with 14-μm particles, which were hollow plastic spheres with a metallic coating. Images of the velocity field were recorded by a digital camera with a resolution of 1008×1018 pixels. A frame-to-frame cross-correlation technique was employed to determine the value of velocity for a given

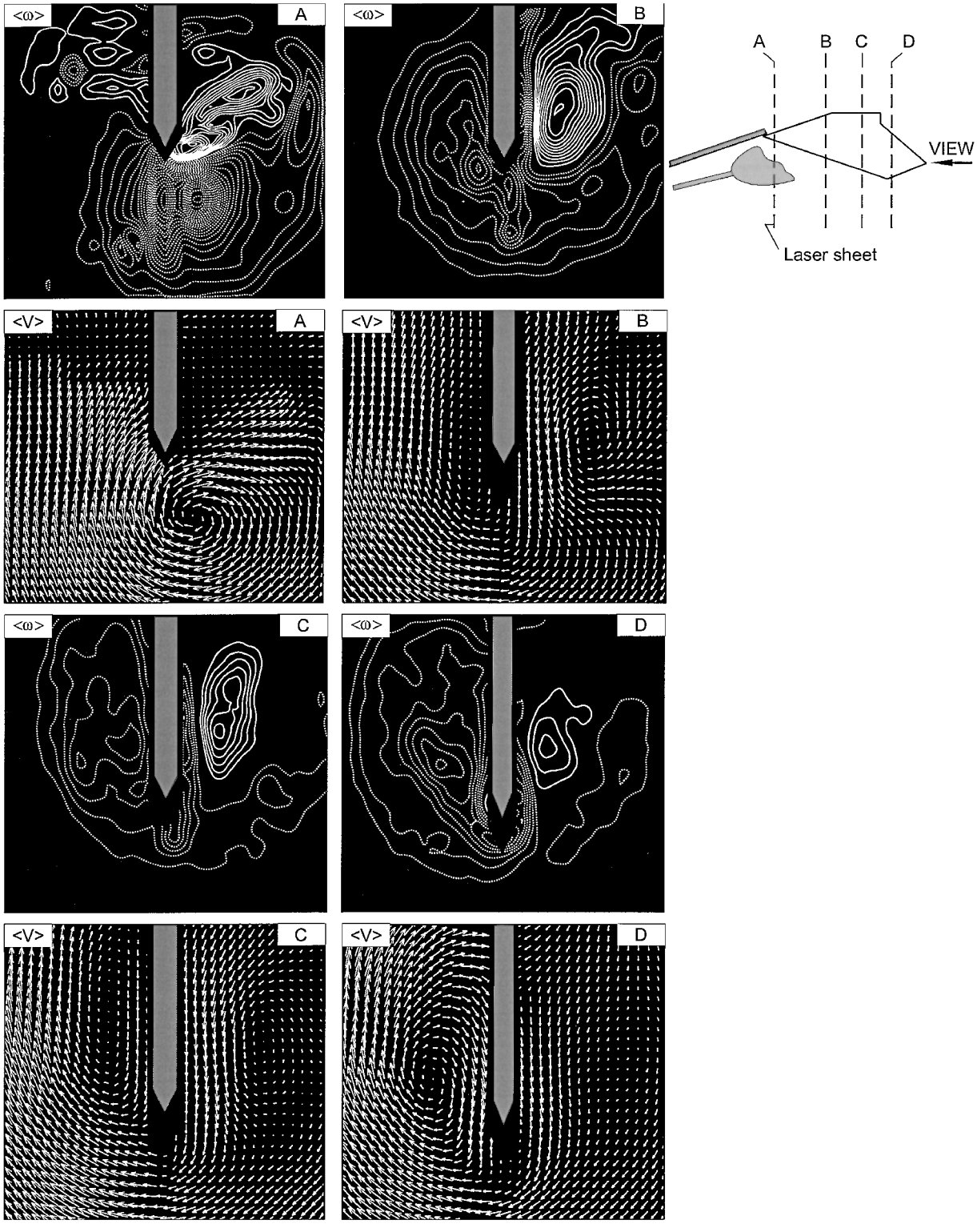

Fig. 2 Averaged vorticity $\langle\omega\rangle$ and averaged velocity $\langle V\rangle$ on planes *A*, *B*, *C*, and *D*, for which $\langle\omega\rangle_{\min} = \pm 1\ \mathrm{s}^{-1}, \pm 1\ \mathrm{s}^{-1}, \pm 2\ \mathrm{s}^{-1}, \pm 1\ \mathrm{s}^{-1}$, respectively, and for which $\Delta\langle\omega\rangle = 1\ \mathrm{s}^{-1}$ (all planes).

interrogation window, which had dimensions of 32 × 32 pixels. Use of this interrogation window, along with a 50% overlap to satisfy the Nyquist criterion, gave an effective grid size of 2.1 mm in the plane of the laser sheet. The magnification factor was $M = 1{:}7.54$.

Instantaneous patterns of velocity and vorticity are presented herein. In addition, time-averaged patterns of velocity V, vorticity ω, rms velocity fluctuation and Reynolds stress were obtained from a sequence of 138 images.

Time-Averaged Patterns of Velocity and Vorticity

Time-averaged representations of vorticity $\langle\omega\rangle$ and velocity $\langle V\rangle$ are shown for the laser sheet locations A, B, C, and D in Fig. 2. In image A, it is evident that, in addition to the primary negative (dashed line) vortex incident on the tail, a well-defined secondary (solid line) vortex is formed from the leading edge of the tail. The dimensionless circulation of the secondary vortex is $\Gamma^* = \Gamma/\pi C_T U = 0.0554$; for the primary vortex, $\Gamma^* = -0.2889$. The circulation of the secondary vortex is, therefore, 19% of the circulation of the primary vortex.

The physical mechanism for generation of this secondary vortex is separation from the edge of the tail, which is evident in the corresponding $\langle\omega\rangle$ pattern in image A. That is, a region of very high velocity gradient, typical of a separated shear layer, forms on the right (outboard) side of the tail. The locus of maximum vorticity is coincident with the region of large velocity gradient. This clearly defined mechanism of secondary vortex formation is, therefore, the genesis of the patch of secondary vorticity evident in the investigation of Canbazoglu et al.,[8] as well as in the qualitative visualization of Washburn et al.[16]

Farther downstream, in image B, the process of formation of the secondary vortex is complete. In fact, a well-defined layer of negative vorticity exists between the secondary vortex and the surface of the tail. Furthermore, a larger region of primary (negative) vorticity now exists on the left (inboard) side of the tail. The swirl patterns associated with this primary vortex, as well as with the secondary vortex, are evident in the $\langle\omega\rangle$ pattern in image B.

Further development of the patterns of primary and secondary vorticity is indicated in images C and D of Fig. 2. It is evident that the secondary vortex remains at approximately the same location on the right (outboard) side of the tail in images C and D. Furthermore, the intensity of the swirl pattern on the right (outboard) side of the tail becomes more focused in going from image C to image D. It is evident in images B–D that both the magnitude of the peak vorticity and the circulation of the secondary vortex decrease with streamwise distance. The respective values of dimensionless circulation are $\Gamma^* = 0.0804$, 0.0394, and 0.0136.

Instantaneous Patterns of Vorticity

Representative patterns of instantaneous vorticity on planes A–D are given in Fig. 3. They can be directly compared with the corresponding patterns of averaged vorticity $\langle\omega\rangle$ shown in Fig. 2. In image A, the instantaneous pattern shows relatively little deviation from the time-averaged pattern given in Fig. 2. In image B, the

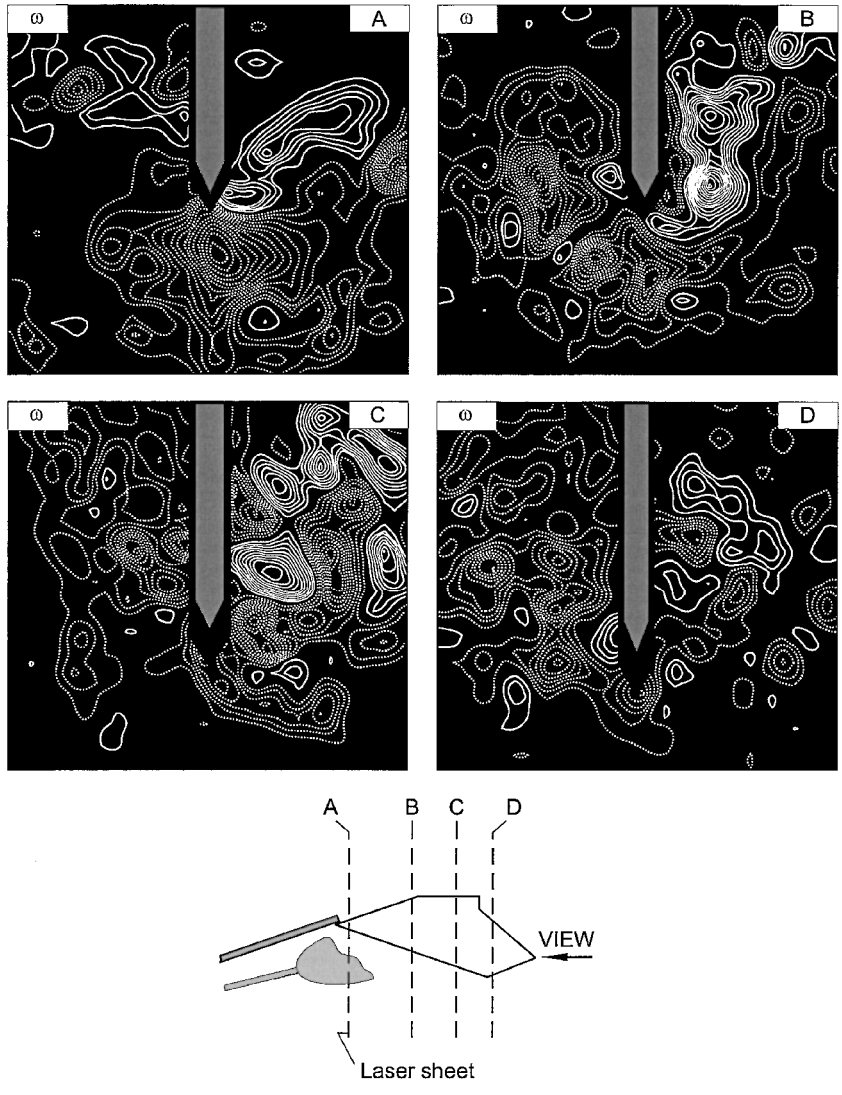

Fig. 3 Instantaneous vorticity ω on planes A, B, C, and D; on all planes, minimum and incremental values of vorticity are $\omega_{min} = \pm 2\ s^{-1}$ and $\Delta\omega = 2\ s^{-1}$.

instantaneous pattern is generally similar to the averaged pattern of Fig. 2. The appearance of a number of small-scale clusters of instantaneous vorticity in image *B* of Fig. 3 is, however, not evident in the pattern of averaged vorticity in image *B* of Fig. 2. Farther downstream, corresponding to images *C* and *D* in Fig. 3, the patterns of instantaneous vorticity show large deviations from the corresponding averaged patterns of Fig. 2. In fact, the well-defined secondary vortex in the averaged *C* and *D* images of Fig. 2 cannot be identified in the instantaneous images *C* and *D* in Fig. 3. This observation indicates that the vortex structure becomes less coherent at larger streamwise distances along the tail.

Averaged Patterns of Velocity Fluctuation and Reynolds Stress

Figures 4 and 5 show contours of constant rms velocity fluctuation w_{rms} and v_{rms}, as well as patterns of the Reynolds stress correlation $\langle w'v' \rangle$, on planes *A* and *D*, which correspond to the leading and trailing regions of the tail.

In Fig. 4, the patterns of w_{rms} and v_{rms} show peak values at the locations designated by the points a_1 and a_2. The corresponding points on the images of averaged vorticity $\langle \omega \rangle$ and averaged velocity $\langle V \rangle$ are represented, respectively, by $a_{1\omega}$ and $a_{2\omega}$ and a_{1V} and a_{2V}. It is evident that regions of high fluctuation intensity occur at the interface between the primary and secondary vortices. Furthermore, the plot of Reynolds stress $\langle w'v' \rangle$ shown in Fig. 4e shows a number of positive and negative peaks. Four of these peaks, designated as a_1^-, a_2^+, a_4^+, and a_5^+, lie close to the interface between the primary and secondary vortices, that is, in the region of high shear. A fifth, lower level peak, designated as a_3^+, occurs at the far edge of the cluster of secondary vorticity. It is, therefore, evident that the process of formation of the secondary vortex, which involves flow separation and a region of large velocity gradient, generates large fluctuations.

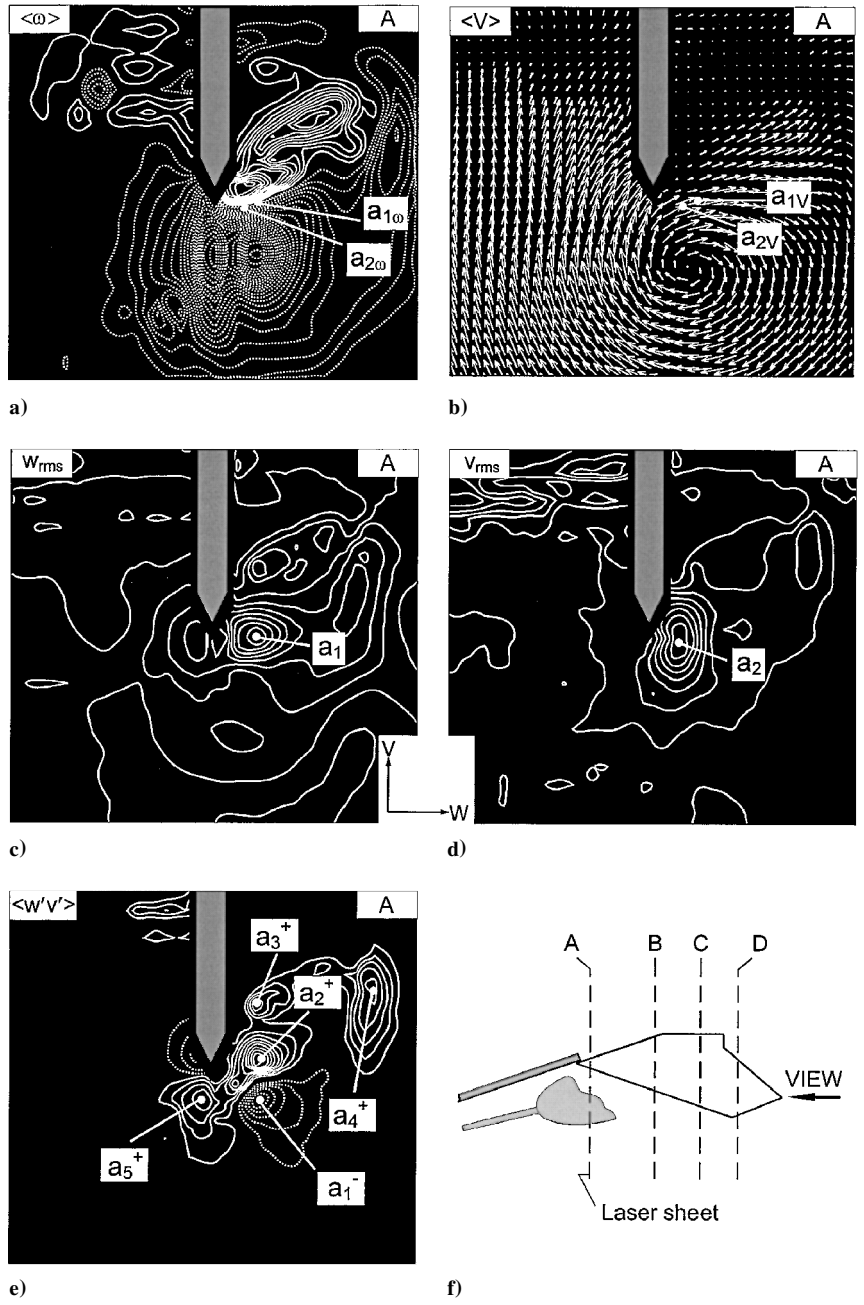

Fig. 4 Averaged a) vorticity $\langle \omega \rangle$, b) velocity $\langle V \rangle$, rms values of velocities c) w_{rms} and d) v_{rms}, and e) Reynolds stress $\langle w'v' \rangle$ on plane *A*; minimum and incremental values of parameters are as follows: $\langle \omega \rangle_{\min} = \pm 1\ \text{s}^{-1}$ and $\Delta\langle \omega \rangle = 1\ \text{s}^{-1}$; $(w_{\text{rms}})_{\min} = 5$ mm/s, and $\Delta\ (w_{\text{rms}}) = 5$ mm/s; $(v_{\text{rms}})_{\min} = 5$ mm/s and $\Delta(v_{\text{rms}}) = 5$ mm/s; and $\langle w'v' \rangle_{\min} = \pm 50\ \text{mm}^2/\text{s}^2$ and $\Delta\langle w'v' \rangle = 50\ \text{mm}^2/\text{s}^2$.

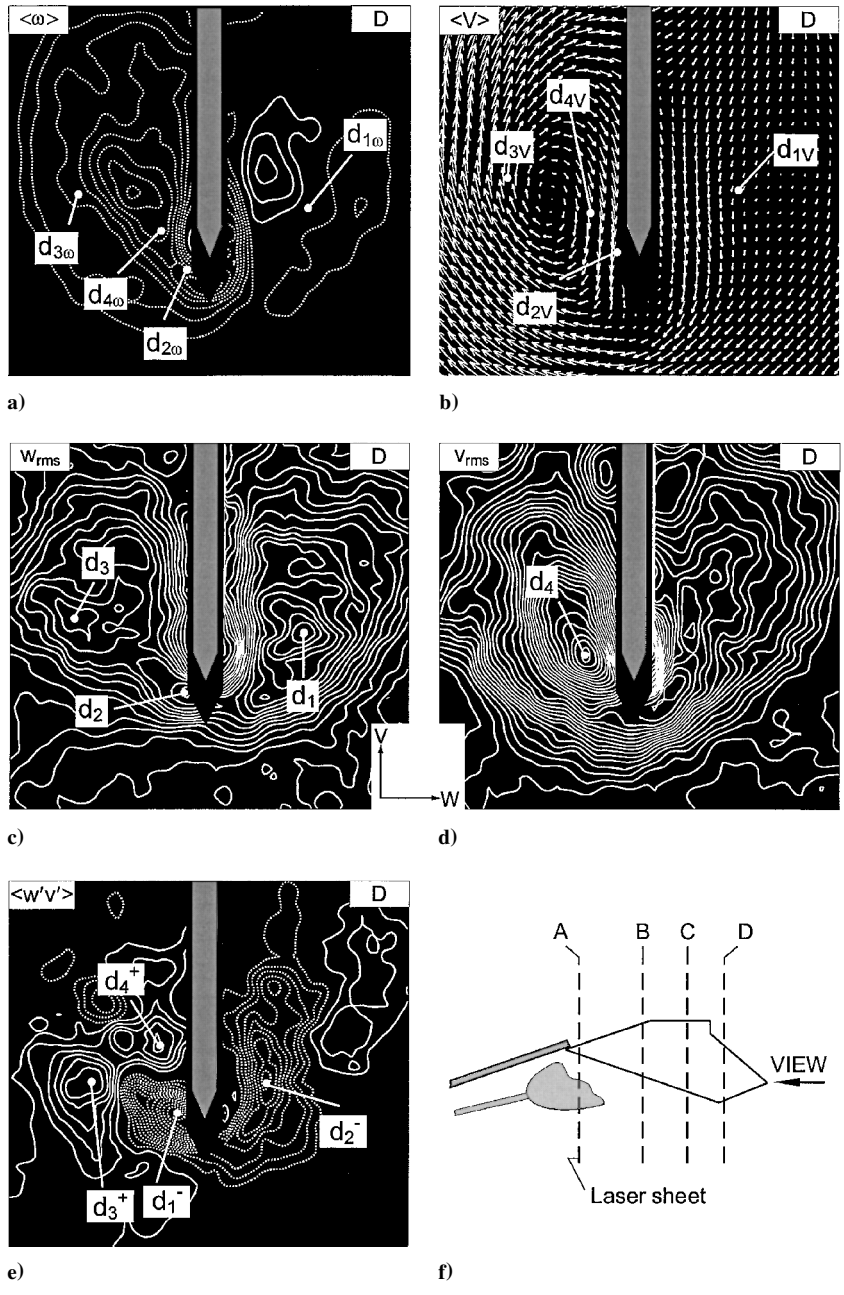

Fig. 5 Averaged a) vorticity $\langle\omega\rangle$, b) velocity $\langle V\rangle$, rms values of velocities c) $w_{\rm rms}$ and d) $v_{\rm rms}$, and e) Reynolds stress $\langle w'v'\rangle$ on plane D; minimum and incremental values of parameters are as follows: $\langle\omega\rangle_{\rm min} = \pm 1\ {\rm s}^{-1}$ and $\Delta\langle\omega\rangle = 1\ {\rm s}^{-1}$; $(w_{\rm rms})_{\rm min} = 1$ mm/s and $\Delta(w_{\rm rms}) = 1$ mm/s; $(v_{\rm rms})_{\rm min} = 1$ mm/s and $\Delta(v_{\rm rms}) = 1$ mm/s; and $\langle w'v'\rangle_{\rm min} = \pm 20\ {\rm mm}^2/{\rm s}^2$ and $\Delta\langle w'v'\rangle = 20\ {\rm mm}^2/{\rm s}^2$.

Figure 5 shows the corresponding patterns in the trailing region of the tail, that is, on plane D. The peak value of $w_{\rm rms}$ occurs at location d_1; it is indicated as $d_{1\omega}$ in the image of $\langle\omega\rangle$. In other words, the locus of this peak is at the interface between the primary and secondary regions of vorticity. Additional peaks in the fluctuating velocity field are identifiable at locations d_2 and d_3 in the image of $w_{\rm rms}$ and d_4 in the image of $v_{\rm rms}$. The corresponding locations of these peaks are at $d_{2\omega}$, $d_{3\omega}$, and $d_{4\omega}$ in the image of averaged vorticity $\langle\omega\rangle$ and at d_{2V}, d_{3V}, and d_{4V} in the image of averaged velocity $\langle V\rangle$ on plane D in Fig. 5. All of these peaks are associated with the distortion of the primary vortex on the left (inboard) side of the tail as it is swept about the tip of the tail. As regards the pattern of Reynolds stresses, an identifiable peak d_2^- occurs at a location approximately corresponding to the interface between the primary and secondary clusters of vorticity on the right (outboard) side of the tail. The remaining three peaks designated as d_1^+ and d_3^+ on the image of $\langle w'v'\rangle$ occur along the shear layer that feeds into the primary vortex as it is distorted past the edge of the tail. An additional peak d_4^+ occurs between the center of the primary vortex and the surface of the tail.

When the images of Figs. 4 and 5 are viewed together, the peak values of the transverse velocity fluctuations are, respectively, $w_{\rm rms}/U = 0.296$ and 0.138. Correspondingly, the peak values of the vertical velocity fluctuation are $v_{\rm rms}/U = 0.263$ and 0.224. The peak value of Reynolds stress is $\langle w'v'\rangle/U^2 = 0.019$ in image A of Fig. 4, whereas its corresponding value is $\langle w'v'\rangle/U^2 = 0.005$ in image D of Fig. 5. The values of generated Reynolds stress are, therefore, much larger during the initial stage of vortex–tail interaction, which involves generation of the secondary (counter) vortex.

Conclusions

Interaction of a broken-down vortex with the leading edge of a tail results in formation of a pronounced secondary vortex of opposite sign. The primary vortex induces a separated shear layer from the leading edge of the tail, which gives rise to this secondary (counter)

vortex. Its circulation is on the order of one-fifth of the circulation of the primary (incident) vortex.

Near the leading region of the tail, the primary–secondary (counter) vortex system is highly coherent. The instantaneous vortex patterns deviate only slightly from the time-averaged representations. Furthermore, locations of peak values of velocity fluctuation and Reynolds stress occur at the interface between the primary and secondary vortices on the outboard side of the tail.

Evolution of this vortex pattern along the tail is associated with a degeneration of coherence of the primary–secondary vortex system. That is, the instantaneous states deviate significantly from the time-averaged pattern of the primary–secondary vortex system.

In the trailing region of the tail, peak values of velocity fluctuation and Reynolds stress are still detectable at the interface between the primary and secondary vortex on the outboard side of the tail. However, in addition, severe distortion of the primary vortex about the tail results in additional peaks of velocity fluctuation and Reynolds stress on the inboard side.

Acknowledgments

The authors gratefully acknowledge support of this research under U.S. Air Force Office of Scientific Research Grants F49620-00-1-0009 and F49620-02-1-0061, monitored by Steven Walker and John Schmisseur. In addition, supplemental funding for instrumentation was provided by U.S. Office of Naval Research Grants N00014-99-1-0581 and N0014-01-1-0606.

References

[1]Rockwell, D., "Vortex Body Interactions," *Annual Review of Fluid Mechanics*, Vol. 30, 1998, pp. 199–229.

[2]Menke, M., and Gursul, I., "Unsteady Nature of Leading Edge Vortices," *Physics of Fluids*, Vol. 9, No. 10, 1997, pp. 2610–2616.

[3]Garg, A. K., and Leibovich, S., "Spectral Characteristics of Vortex Breakdown Flowfields," *Physics of Fluids*, Vol. 22, No. 11, 1979, pp. 2053–2064.

[4]Gursul, I., "Unsteady Flow Phenomena over Delta Wings at High Angle of Attack," *AIAA Journal*, Vol. 32, No. 2, 1994, pp. 225–231.

[5]Gursul, I., and Yang, H., "On Fluctuations of Vortex Breakdown Location," *Physics of Fluids*, Vol. 7, No. 1, 1995, pp. 229–231.

[6]Beutner, T. J., Baust, H. N., and Meyers, J. F., "Doppler Global Velocimetry Measurements of a Vortex–Tail Interaction," *Proceedings of the 7th International Symposium on Flow Visualization*, edited by J. P. Crowder, Begell House, New York, 1995, pp. 418–423.

[7]Canbazoglu, S., Lin, J.-C., Wolfe, S., and Rockwell, D., "Buffeting of Fin: Distortion of Incident Vortex," *AIAA Journal*, Vol. 33, No. 11, 1995, pp. 2144–2150.

[8]Canbazoglu, S., Lin, J.-C., Wolfe, S., and Rockwell, D., "Buffeting of Fin: Streamwise Evolution of Flow Structure," *Journal of Aircraft*, Vol. 33, No. 1, 1995, pp. 185–190.

[9]Rizk, Y. M., and Gee, K., "Unsteady Simulation of Viscous Flowfield Around F-18 Aircraft at Large Incidence," *Journal of Aircraft*, Vol. 29, No. 6, 1992, pp. 986–992.

[10]Gee, K., Murman, S. M., and Schiff, L. B., "Computational Analysis of F/A-18 Tail Buffet," AIAA Paper 95-3440, Aug. 1995.

[11]Kandil, O. A., Sheta, E. F., and Massey, S. J., "Buffet Responses of a Vertical Tail in Vortex Breakdown Flows," AIAA Paper 95-3464, Aug. 1995.

[12]Rizzetta, D. P., "Numerical Simulation of the Interaction Between a Leading-Edge Vortex in a Vertical Tail," AIAA Paper 96-2012, June 1996.

[13]Wolfe, S., Canbazoglu, S., Lin, J.-C., and Rockwell, D., "Buffeting of Fins: Assessment of Surface Pressure Loading," *AIAA Journal*, Vol. 33, No. 11, 1995, pp. 2232–2235.

[14]Mayori, A., and Rockwell, D., "Interaction of a Streamwise Vortex with a Thin Plate: A Source of Turbulent Buffeting," *AIAA Journal*, Vol. 32, No. 10, 1994, pp. 2022–2029.

[15]Gordnier, R. E., and Visbal, M. R., "Numerical Simulation of the Impingement of a Streamwise Vortex on a Plate," AIAA Paper 97-1781, June–July 1997.

[16]Washburn, A. E., Jenkins, L. M., and Ferman, M. A., "Experimental Investigation of Vortex–Fin Interaction," AIAA Paper 93-0050, Jan. 1993.

A. Plotkin
Associate Editor

Autonomous Gain-Phase Tailoring of Rotational Acceleration Rate Sensors

Yu-Hsiang Hsu* and Chih-Kung Lee†
National Taiwan University,
Taipei 106, Taiwan, Republic of China

Nomenclature

c	=	elastic stiffness constants
D	=	electric displacement
d	=	piezoelectric strain/charge constant
E	=	electrical field
e	=	piezoelectric stress/charge constant
G	=	shear modulus
k	=	wave number
q	=	surface charge
r	=	radius of the shaft
S	=	strain
T	=	stress
u	=	displacement along x direction
v	=	displacement along y direction
ε	=	permittivity
θ	=	twisting angle
ρ	=	density
ω	=	frequency

Introduction

THE original concept of spatial filter, first reported in 1990,[1] was based on a distributed piezoelectric sensor that introduced a no-phase delay low-pass filter to the sensor transfer function. This spatial filter could only be placed far from the boundaries of a free-free plate and was required to be smaller in size when compared with the attached structure. The underlying reason for the spatial filter to be placed at locations far from the boundaries was to avoid the effect of evanescent waves and the effect of the boundaries, that is, only propagating waves were to be considered. Even with those restrictions, these earlier spatial filters did successfully introduce a no-phase delay low-pass filter to the sensor transfer that at first glance seems to conflict with the Bode gain-phase theorem. More specifically, spatial filters appear to offer a valid approach to introducing autonomous behavior into sensor transfer functions. As a rod can be modeled by using a second-order partial differential equation, only two propagating waves are needed to examine their dynamic behaviors.[2] A newly developed methodology that extends the earlier spatial wave concept to include finite structures or structures with sizes comparable to that of the sensor size will be introduced. With the capability to handle boundary effects and then utilizing the fact that only propagating wave modes are present within a rod, a rotational acceleration rate sensor that uses a rod as its base structure was developed to demonstrate bandwidth expansion capabilities when a distributed sensor design is integrated with a traditional point sensor. The theory, experimental results, related design, and performance implications on this newly invented rotational acceleration rate sensor will be detailed in this Note.

Theory of Piezoelectric Laminates

The constitutive equations of piezoelectric materials are[3]

$$S_p = s^E_{pq} T_q - d_{ip} E_i, \qquad D_i = d_{ip} T_q + \varepsilon^T_{ij} E_k \tag{1}$$

Received 24 August 2001; revision received 10 April 2002; accepted for publication 17 April 2002.

*Graduate Research Assistant, Institute of Applied Mechanics.
†Professor, Institute of Applied Mechanics. Senior Member AIAA.